Investigation of ion and electron heat transport of high-T_e ECH heated discharges in the Large Helical Device

N.A. Pablant,[1] S. Satake,[2,3] M. Yokoyama,[2,3] D.A. Gates,[1] M. Bitter,[1] N. Bertelli,[1] L. Delgado-Aparicio,[1] A. Dinklage,[4] M. Goto,[2] K.W. Hill,[1] S. Igamai,[2] S. Kubo,[2] S. Lazerson,[1] S. Matsuoka,[5] D.R. Mikkelsen,[1] S. Morita,[2,3] T. Oishi,[2,3] R. Seki,[2] T. Shimozuma,[2] C. Suzuki,[2] Y. Suzuki,[2,3] H. Takahashi,[2] H. Yamada,[2,3] Y. Yoshimura,[2] and the LHD Experiment Group

[1)] *Princeton Plasma Physics Laboratory, Princeton, New Jersey 08543, USA*

[2)] *National Institute for Fusion Science, Toki, Gifu 509-5292, Japan*

[3)] *SOKENDAI (The Graduate University for Advanced Studies), Toki, Gifu 509-5292 Japan*

[4)] *Max-Planck-Institut für Plasmaphysik, Greifswald, Germany*

[5)] *Research Organization for Information Science and Technology, Kobe, Hyogo 650-0047, Japan*

(Dated: 1 December 2015)

ABSTRACT

An analysis of the radial electric field and heat transport, both for ions and electrons, is presented for a high-T_e electron cyclotron heated (ECH) discharge on the Large Helical Device (LHD). Transport analysis is done using the TASK3D transport suite[1] utilizing experimentally measured profiles for both ions and electrons. Ion temperature and perpendicular flow profiles are measured using the recently installed x-ray imaging crystal spectrometer diagnostic (XICS)[2], while electron temperature and density profiles are measured using Thomson scattering. The analysis also includes calculated ECH power deposition profiles as determined through the TRAVIS ray-tracing code. This is the first time on LHD that this type of integrated transport analysis with measured ion temperature profiles has been performed without NBI injection, allowing the heat transport properties of plasmas with only ECH heating to be more clearly examined. For this study, a plasma discharge is chosen which develops a high central electron temperature ($T_{eo} = 9keV$) at moderately low densities ($n_{eo} = 1.5 \times 10^{19} m^{-3}$). The experimentally determined transport properties from TASK3D are compared to neoclassical predictions as calculated by the GSRAKE and FORTEC-3D codes. The predicted electron fluxes are seen to be an order of magnitude less than the measured fluxes, indicating that electron transport is largely anomalous, while the neoclassical and measured ion heat fluxes are of the same magnitude. Neoclassical predictions of a strong positive ambipolar electric field (E_r) in the plasma core are validated through comparisons to perpendicular flow measurements from the XICS diagnostic. This provides confidence that the predictions are producing physically meaningful results for the particle fluxes and radial electric field, which are a key component in correctly predicting plasma confinement.

I. INTRODUCTION

In stellarator plasmas, it is possible to develop plasmas with high central electron temperatures in low collisionality plasmas through the use of electron cyclotron heating (ECH)[3]. These conditions are associated with core electron-root confinement (CERC) plasmas[4], which develop a region of positive electric field and reduced electron heat transport in the central region of the plasma. The core electron-root formation is due to a 3D-specific bifurcation of the ambipolarity condition at low collisionalities. This reduction in transport leads to a peaking of the electron temperature in the core and is known as the high-T_e regime. Plasmas of this type on the Large Helical Device (LHD) have reached central temperatures of greater than $15keV$ in low density conditions, $n_{eo} = 0.2 \times 10^{19} m^{-3}$, and greater than $9keV$ even with densities as high as $n_{eo} = 1.5 \times 10^{19} m^{-3}$.

In these plasmas, neoclassical predictions based on the condition of ambipolar fluxes predict a positive radial electric field (electron-root solution) across the core region of the plasma when in the high-T_e regime, while a negative electric field is otherwise expected. Previous studies have reported that a transition from the ion-root phase to the electron-root phase requires a minimum ratio of input power to density. An understanding of the applicability of the neoclassical predictions to these plasmas, as well as the dynamics involved in developing the electron root region, is being actively pursued at LHD.[3,5–10]

In this paper, the analysis of high-T_e plasmas is extended by looking at the detailed evolution of a CERC discharge which is produced using only ECH heating. The analysis of the transport and radial electric field structure is performed with the TASK3D transport suite along with measurements of the perpendicular flow velocity from the high resolution x-ray crystal spectrometer (XICS)[2]. For this analysis the ion temperature profiles are taken from the XICS system, and electron temperature profiles are taken from the Thomson scattering system[11]. To determine the ECH heat deposition profile the TRAVIS ray-tracing code[12] is used. Heat transport estimates are made using power balance considerations based on the plasma parameters and calculated power deposition profiles.

This work benefits from the recent installation of the XICS diagnostic which allows, for the first time on LHD, the ion heat transport and perpendicular flow to be measured in the absence of any neutral beam injection. In addition significantly more ECH heating is now available at LHD than in previous studies, allowing CERC plasmas to be accessed without

any additional power sources[10]. These two development enable the study of plasmas that are only heated using ECH. The use of a single source of external heating simplifies power balance calculations and reduces the sources of uncertainties. In addition, neoclassical calculations or simulations of a plasma without momentum input by NBI are significantly easier to perform, and in most neoclassical treatments external momentum drive is neglected. The neoclassical calculations in the current work are more directly comparable with the experimental values since no external momentum input sources are present during the shot evolution.

In the high-T_e discharge studied, an increase in power and decrease in density is found to be associated with an expansion of the positive radial electric field from a well defined core region ($\rho \lesssim 0.3$) to a region covering the majority of the plasma minor radius ($\rho \lesssim 0.8$). Access to this global electron-root configuration is made possible by the recent upgrades in available ECH power. The structure of the radial electric field, inferred from the perpendicular flow measurements, is compared with neoclassical predictions from the GSRAKE and FORTEC-3D codes. The measurements are in general agreement with the predictions throughout the discharge, which provides confidence in the neoclassical calculations.

The changes in the ion and electron heat fluxes associated with the expansion of the radial electric field are also be examined and compared width neoclassical predictions. These measurements, in a pure ECH plasma, add to previous work on plasmas which also included neutral beam heating and which focused only on the electron heat flux. The current measurements of the perpendicular flow velocity help to clarify the role of the neutral beams in affecting the structure of the radial electric field.

The analysis developed for this study highlights the current capabilities of the TASK3D suite for thermal transport analysis and demonstrates the integration of a set of equilibrium and power deposition codes, providing the base set of tools required for power balance analysis in stellarator geometries.

II. METHODS

A. Shot Evolution

The analysis in this paper is based around an ECH heated discharge from the 16th LHD experimental campaign in 2012. Time traces for shot 114722, are shown in Fig.1. This

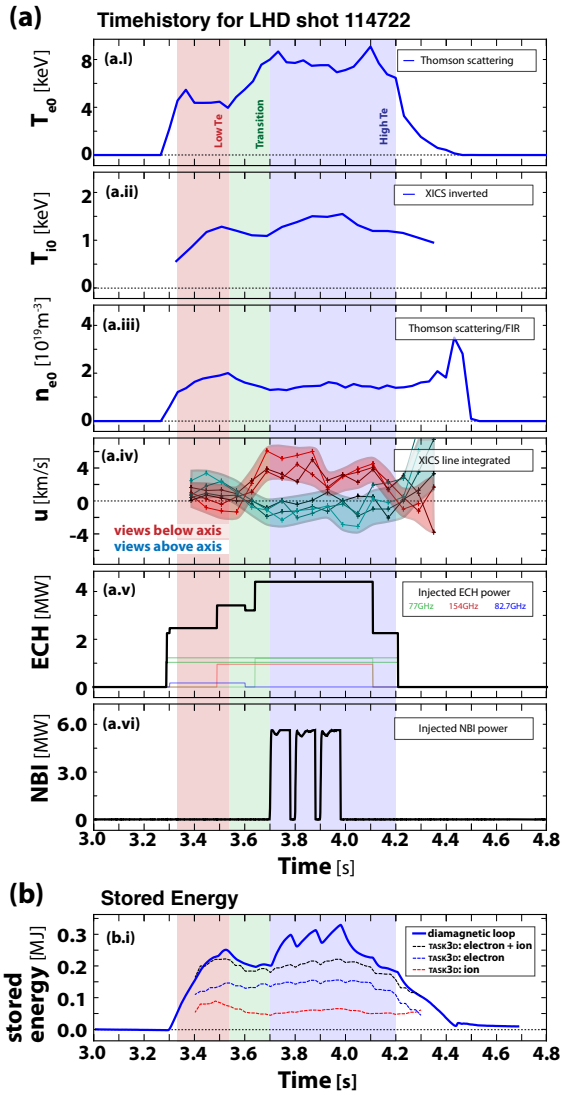

FIG. 1. (a) Time evolution of LHD shot 114722. (a.i) Central electron temperature as measured by Thomson scattering and averaged over the 10 central channels. (a.ii) Inverted central ion temperature from the XICS diagnostic. (a.iii) Central electron density taken from Thomson scattering and normalized to the line integrated measurements from the FIR system. (a.iv) Line integrated plasma flow along the viewing direction, measured by the XICS diagnostic. (a.v) Injected ECH power. The black line represents the total injected power, the colored lines represent individual gyrotrons. (a.vi) Injected NBI power from the perpendicular neutral beam. (b) Time history of the plasma stored energy. The solid blue line is the total stored energy as measured by the diamagnetic loop. The blue and red dashed lines represent kinetic stored energy calculated from the measured temperature and density profiles. The black dashed line shows the total kinetic stored energy found by adding the ion and electron stored energy.

discharge begins as a typical CERC plasma with a transition from a low-T_e phase to high-T_e phase as the ECH heating power is increased. Typical density and temperature profiles during these two phases are shown in Fig.2. In this figure the profiles are plotted against

the normalized minor radius, which is defined as $\rho \equiv \sqrt{\psi/\psi_{edge}}$ where ψ is the toroidal flux enclosed by a given flux surface.

This discharge utilizes an inward shifted configuration with the magnetic axis location set to $3.53m$. The magnetic field on axis is $+2.705T$, which corresponds to the clockwise direction when viewed from the top. During most of this shot, only ECH heating is used, with a peak injected power of $4.4MW$. This heating is achieved using a combination of the three $77GHz$, one $82.7GHz$ and one $154GHz$ systems, and is injected from multiple launcher systems[13].

Starting at $3.5s$ the $154GHz$ Gyrotron is turned on increasing the injected power from $2.5MW$ to $3.4MW$. An additional $77GHz$ system is added at 3.64 seconds raising the injected power to $4.4MW$. During the $200ms$ after the power increase at 3.5 seconds, the plasma transitions from a low-T_e phase to a high-T_e phase. During this transition it can be observed that the line integrated density decreases (from $1.6 \times 10^{19} m^{-3}$ to $1.0 \times 10^{19} m^{-3}$), the electron temperature increases (from $4keV$ to $9keV$), and there is a dramatic change in the perpendicular flow.

While the electron temperature increases dramatically during the transition period, the density loss and reduction in T_i leads to an overall reduction in the total stored energy, a relatively constant electron stored energy, and a strong decrease in the ion stored energy (see Fig.1(b)). During this shot, and in particular around the transition time, a constant gas puffing rate is used (no density feedback) and there is no significant change in any other particle fueling source (except during neutral beam injection).

During the time between 3.7 and $4.0s$, $5.4MW$ of port-through injected neutral beam power is added by one of the $40keV$ perpendicular neutral beams (NBI #5). In the current analysis we focus on the plasma state before the NBI turn on ($3.7s$) and after the NBI turn off and subsequent relaxation of the fast ion distribution ($4.1s$), and therefore do not include the NBI deposition in the calculations.

Correlated with the increase of the central electron temperature after $3.5s$ is a dramatic change in the argon perpendicular flow velocity, as measured by the XICS system. The time evolution of the line integrated perpendicular velocity measurements can be seen in Fig.1(a.iv). The detailed rotation profiles, shown in Fig.3, indicate that during the low-T_e phase there is a core region of the plasma rotating in the negative poloidal direction (ion-diamagnetic drift direction), while the outer portion of the plasma is rotating in the positive

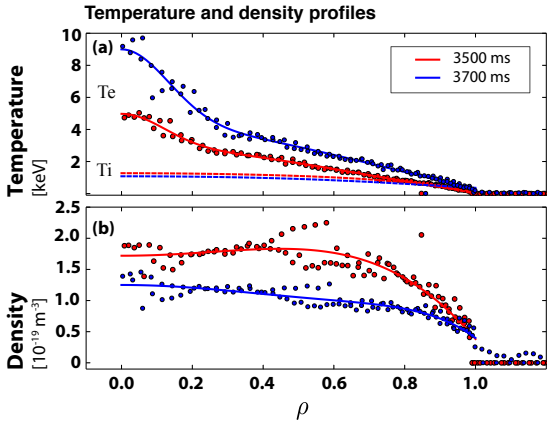

FIG. 2. Temperature and density profiles for 114722 at $3500ms$ and $3700ms$. (a) Electron temperature from the Thomson scattering and inverted ion temperature from the XICS system. (b) Electron density found from Thomson scattering and normalized to the line integrated density reported by the far infrared laser interferometer system (FIR). In all plots the points represent the raw data, and the solid lines represent the fit to the data used in the analysis.

direction. During the transition phase, the rotation inversion radius expands outward, and in the high-T_e phase the entire central plasma (the measurement range is limited to $\rho \leq 0.8$) is rotating in the negative direction. The change in the perpedicular flow is noticable in the first measurement after the transition has started, at $3.570ms$, particularly when looking at the inverted $U_\perp$ profiles. The time resolution for the velocity measurements is limited to $60ms$ for this discharge, so it is not possible to make any cause and effect concusions in the current work. The perpendicular flow and electric field are closely related, and a flow in the ion-diamagnetic drift direction rotation corresponds to a positive radial electric field, as described in Section III.

B. TASK3D

The TASK3D suite has been developed to provide an integrated package for power balance analysis on LHD.[1,14,15] It acts as a framework to integrate multiple codes and calculations, and to provide the necessary data gathering and manipulation to consistently enable transport analysis for 3D geometries. There are numerous modules that can be included as part of the TASK3D framework, however for the current work only a subset of available calculations will be used.

For these initial studies a simplified transport model is used that only considers ECH

power deposition, local collisional temperature equilibration between electrons and the main ions (hydrogen), time evolution of the temperature and density profiles, and the heat transport across flux surfaces. TASK3D performs a simple power balance calculation in which all deposited power must be either radially transported across flux surfaces to the plasma edge, or must contribute to the evolution of the stored energy profile. Some significant simplifications will be used such as assuming $n_e = n_i$ across the entire profile, and neglecting any radiative losses.

For the analysis done in this paper, pyTASK3D was developed as a alternative front end for the TASK3D suite. This package handles preparation of the diagnostic profiles and integration of the analysis modules. The development of pyTASK3D was done as part of a collaborative effort between NIFS and PPPL.

C. Diagnostic Profiles

In order to carry out the transport analysis, accurate measurement of the ion and electron temperature profiles are required. The XICS diagnostic, installed in 2011 and upgraded in 2012, allows, for the first time on LHD, for full ion temperature profiles to be measured in the absence of neutral beam injection.

The XICS diagnostic provides line integrated measurements of the plasma ion temperature and flow velocity profile based on emission from trace amounts of highly charged argon (Ar^{16+}). These line-integrated measurements are then inverted, using tomographic inversion techniques, to recover the true temperature and rotation profiles as a function of the flux coordinate. This inversion process assumes that the argon emissivity and temperature are constant on flux surfaces. A smooth spline representation for the final ion temperature is enforced as part of the inversion process used for the XICS profiles.The details of the diagnostic operation and inversion techniques are described in Ref. 2,16.

For the current work, the techniques used for the velocity inversion have been improved to account for the expected spatial dependence of the perpendicular flow. The parallel flow is defined as being in the direction of the local magnetic field lines, and the perpendicular flow direction to be in the $\nabla\rho \times \boldsymbol{B}$ direction. A simple form for the variation of the perpendicular flow on a flux surface can now be found from the radial force balance equation (see Section III) given the assumption that the plasma potential and plasma pressure are flux surface

functions. With these assumptions the local perpendicular flow, $\boldsymbol{u}_\perp$, can be related to the flux surface average flow, $U_\perp$, by the following expression:

$$\boldsymbol{u}_\perp = \boldsymbol{f} U_\perp, \quad \boldsymbol{f} = -\frac{\langle \boldsymbol{B} \rangle}{\langle |\nabla \rho| \rangle} \left(\frac{\boldsymbol{B} \times \nabla \rho}{B^2} \right) \tag{1}$$

Where $\langle \cdot \rangle$ denotes a flux surface average. Additional details on the derivation of this expression and its applicability are given in Ref. 17.

The XICS system, which has a viewing geometry that is nearly radial, is insensitive to parallel flow near the magnetic axis and only weakly sensitive towards the outer portions of the plasma. In addition, the parallel flow is expected to small in LHD plasmas with no external momentum input. While in principle it is possible for the XICS system to resolve both parallel and perpendicular flow (given that the system sees both above and below the magnetic axis), such measurements are not practical given the weak sensitivity to parallel flow. Instead an assumption is made that the contribution of the parallel flow to the measured XICS flow is negligible and this is assumption is checked by looking at the goodness of fit during the inversion process. The assuptions on the flow variations and absence of parallel flow are at least consistent with the measured data, as can be determined by comparing the line integrated data and the reintegrated final profiles. The measured data is also fully consistent with the assumption that the argon density is constant on flux surfaces and with constraints placed on the Ti profile shape, which are described in Ref. 16. In the case of the ion temperatures, the line integrated and inverted profiles are quite similar and very well constrained; in such a case any mismatch in the assumptions and the final profile would be very obvious in the residual function.

Electron temperature profiles are measured by the Thomson scattering system[11]. For the electron density the profile measured by Thomson scattering is normalized to match the line integrated density measured by the Far Infrared Reflectometer (FIR) system[18]. The temperature and density profiles are then filtered to remove bad channels based on median filtering of the time history of each channel.

Before using any of the diagnostic data in the transport calculations, the profiles are fitted using a smooth function. Several profile representations are implemented in TASK3D which can be used to fit the raw diagnostic data. The choice of the profile representation forces a structure onto profiles which affects the detailed calculations of the diffusion coeffi-

cients. While the overall conclusions from this analysis do not depend on the profile fitting function, the detailed shape of the diffusion coefficient profiles vary slightly depending on which representation is used. The two profile shapes that have been compared in the course of this analysis are a Gaussian plus polynomial representation and a cubic spline representation. The results shown in this paper are based on the fits shown in Fig.2. Fitting against normalized minor radius, ρ, is done using a Gaussian plus polynomial representation with a sixth degree even polynomial. In the current work the uncertainties in the measurements of T_e and n_e are not well characterized, and therefore the profiles are fit without weighting. For T_i and $U_\perp$, the profiles are found through a tomographic inversion algorithm which takes into account both experimental and algorithmic uncertainties.[16]

Since the ion temperature used in the current analysis is based on measurement of the argon temperature, it is important to consider whether thermal equilibration with the main ions (hydrogen) can be expected. A simple 3 species transport model (hydrogen, carbon, argon) has been constructed that confirms that the impurity temperatures are expected to closely match the hydrogen temperatures for the conditions in this plasma shot. In this simple model all heat exchange coefficients between electrons and the three ion species (including exchange between ion species) have been calculated; external heating is assumed to be applied to the electrons (consistent with pure ECH heating) and steady state solutions are found. The impurity densities are estimated, however for these conditions the results are insensitive to the specific densities used.

D. Equilibrium reconstruction

A reconstruction of the 3D plasma equilibrium is required as part of the TASK3D analysis for both calculations of the plasma volume and shape, as well as for the mapping of the various diagnostic measurement locations to a effective minor radius. This same equilibrium is also used to invert the line-integrated XICS measurements and determine the local ion temperature and rotation profiles.[16]

The standard approach in stellarators and heliotrons is to model the plasma equilibrium as a set of nested flux surfaces through the use of the VMEC code[19]. The assumption of nested flux surfaces provides a good model for the equilibrium over most of the plasma volume. In the plasma edge, the true plasma equilibrium is expected to become stochastic, however the

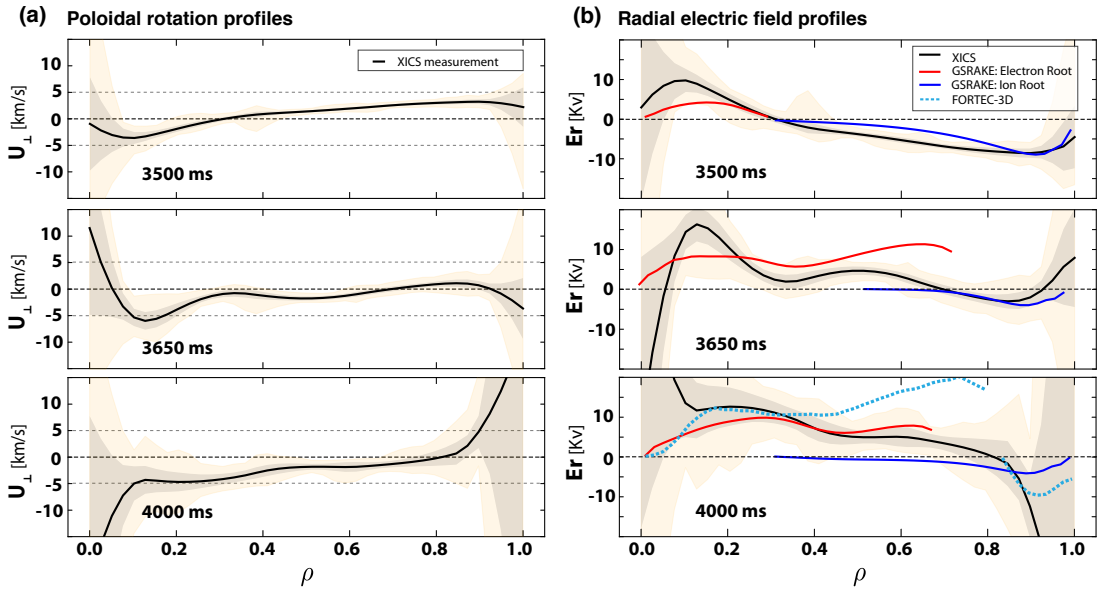

FIG. 3. (a) Argon perpendicular flow profiles (flux surface averaged) as measured by the XICS diagnostic. Profiles are found through tomographic inversion of the line integrated spectral measurements. Shaded regions represent the approximate error in the final inverted profile due to photon statistics. The gray shaded region represents the standard deviation, while the yellow region represents the extreme solutions consistent with the measurements. (b) Radial electric field profiles. The red line represents the GSRAKE electron root solution, the blue line represents the GSRAKE ion root solution, and the dashed cyan line represents the FORTEC-3D solution. The radial electric field inferred from the flow velocity ($E_r = -u_\perp B$) is also shown.

general plasma shape is still reasonably approximated by the VMEC model.

The VMEC code produces an equilibrium based on a set of fixed inputs. To find an equilibrium that matches a particular plasma, a reconstruction technique is needed. For the current work the STELLOPT reconstruction tool was used for equilibrium reconstruction. STELLOPT uses a minimization technique to determine a VMEC equilibrium that best matches the available diagnostic data.[20,21]. This is done by optimizing the pressure profile, toroidal current profile, total enclosed toroidal flux and a pressure scaling factor that are used in a free boundary VMEC equilibrium calculation. For the current reconstructions, the following measurements were targeted: flux loop measurements, electron temperature profile, electron density profile, total stored energy, and total toroidal current.

E. Power deposition and stored energy evolution

Our final transport estimates are based on a power balance calculation that includes only the ECH power deposition and the collisional thermal equilibration between electrons and the main ion (hydrogen).[22] The time dependent evolution of the ion and electron stored energy (energy density evolution) is available for inclusion as part of the TASK3D, however due to the lack of time resolution and uncertainties in the diagnostic profiles this is not included in the current calculation. No other sources of power deposition or loss are considered in this current analysis. The calculated heat deposition, thermal equilibration and stored energy evolution profiles are shown in Fig.4.

In the current version of TASK3D the stored energy evolution is handled by creating an effective power deposition profile that takes into account the time dependent change in the temperature and density profiles. This energy density evolution profile is found using simple differences between adjacent fitted pressure profiles. For both the ions and the electrons, there is not enough diagnostic time resolution (or a long enough steady state period) to accurately calculate these evolution profiles. The inclusion of the stored energy evolution would add a great deal of uncertainty and make drawing conclusions from the ion power balance calculation difficult; for this reason it is neglected in the final power balance calculations. It is nonetheless useful to examine the stored energy evolution profiles, to gauge the possible impact than neglecting them may have.

For the electrons, the stored energy evolution is an order of magnitude less than the ECH power deposition, and will have a negligible effect on the power balance calculations. For the ion stored energy evolution the picture is less clear. Power balance calculations are performed before and after the neutral beam injection which is active between $3.7s$ and $4.0s$. Because of the NBI injection (and subsequent ion slowing down), the ion heating around the analysis times is not constant long enough to make accurate measurements of the ion energy density evolution given the T_i time resolution of $60ms$. However, given that the ion temperature profiles are nearly identical before and after the NBI heating, and the electron temperature and density are relatively constant during the High-T_e phase, it seems reasonable to expect that without the neutral beams, only small changes in the ion stored energy would have been expected between $3.7s$ and $4.1s$. Such an assumption is at least consistent with the time history of the kinetic stored energy, shown in Fig.1(b). The calculated energy density

evolution based on adjacent time slices is shown in Fig.4 as upper bounds, along with the expected energy evolution calculated using only the time slices before and after the NBI injection.

Calculation of the ECH deposition profile has been done using ray-tracing techniques. There are two available ray-tracing codes that have been used for this calculation: TRAVIS[12] and LHDGAUSS[23,24]. TRAVIS is a generalized code for electron cyclotron propagation in 3D geometry, and has been applied to several stellarator systems. The LHDGAUSS code has been specifically developed at NIFS for LHD plasmas. Both codes use a VMEC geometry description and fitted T_e and n_e profiles as the inputs. Separate ray-tracing runs are performed for each combination of launcher, frequency and propagation mode active in the plasma, and then combined based on the expected input power in each case.

Results from the TRAVIS are shown in Fig.4. The results from LHDGAUSS show a qualitatively similar deposition profile, giving us confidence is the accuracy of the calculation implementations. The major uncertainty in these calculated deposition profiles stems from the density profile in the plasma edge. Sufficiently accurate density profiles are not available in this region, requiring extrapolation from Thomson density profile as shown in Fig.2. This lack of information in the edge affects the calculation of the mode fractions (X or O mode) that enter the plasma. The approximation used in the current calculation is that all of the injected power is coupled into the targeted mode. The other major approximation is that only first pass absorption is considered, and the total absorbed power is normalized to the injected power. The ray tracing results show that most of the power is absorbed on the first pass and that this approximation should have a small effect on the accuracy of the results in this case.

During this shot, one of the perpendicular neutral beams is turned on from $3.7s$ to $4.0s$, during the high-T_e period. This $40keV$ neutral hydrogen beam injects approximately $5.4MW$ of port-through power. Inclusion of the NBI in the power balance calculation is possible, but accurate calculations are difficult and require not only the calculation of the initial deposition of fast ions, but also fast ion slowing down, fast ion loss, and electron cooling due to particle fueling. For these reasons we limit our analysis to $3.7s$, before the neutral beam turn on, and $4.1s$ after the neutral beam turn off and subsequent slowing down time. The contribution of the fast ions to total stored energy, as well as the slowing down time, combined with the fast ion confinement time, can be seen experimentally in Fig.1(b).

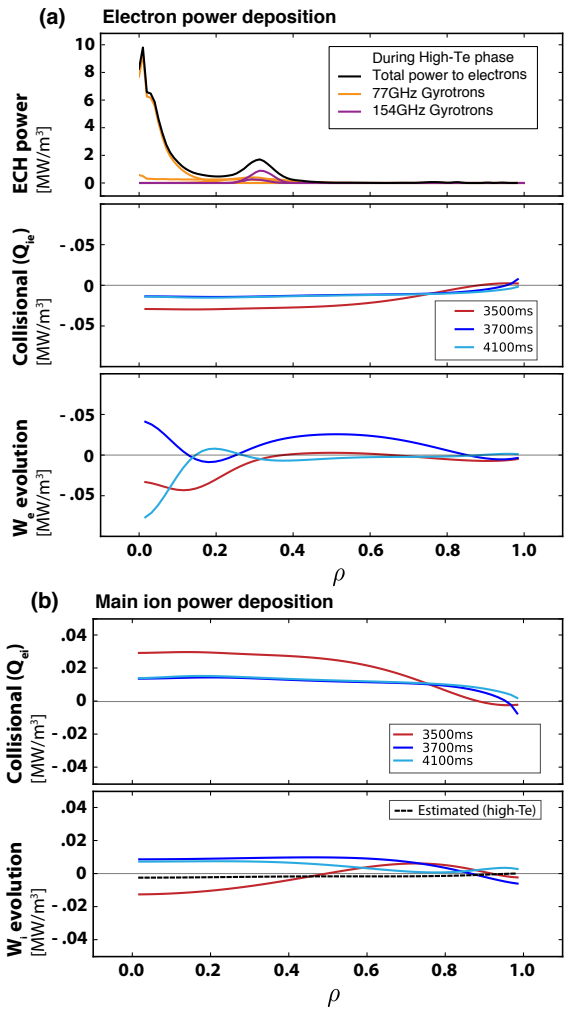

FIG. 4. Power deposition profiles for LHD shot 114722. Profiles for ECH deposition, electron-ion coupling and stored energy evolution are shown. The stored energy evolution profiles are shown here for comparison with the other power deposition profiles but are not included in the final power balance calculation. (a) Electron power deposition. ECH deposition is calculated using the TRAVIS ECH ray-tracing code and includes the three $77GHz$ and the $154GHz$ systems. The ECH deposition profiles are only shown for the high-T_e phase; the low-T_e deposition profile is similar but not as strongly peaked on axis. (b) Main ion power deposition. The dashed line represents the stored energy evolution calculated using only the profiles at $3.7s$ and $4.1s$, at the beginning and end of the High-T_e phase.

Additional information about the evolution of fast-ion distribution created by radial neutral beam injection on LHD can be found in Ref. 25.

The contribution of the core radiated power to the power balance is expected to be small and has not been included in the current power balance calculations. The total radiated power during the analyzed time is approximately $0.4MW$, as measured using the resistive bolometer system[26]. This power loss is far less than the depositied ECH power; furthermore

we would expect the radiated power to be mostly localized in the edge of the plasma, and not significantly affect calculations of the core power balance[27].

F. neoclassical predictions

One of the goals of this analysis is to compare experimentally determined heat fluxes and perpendicular flow profiles with neoclassical predictions, there by gaining some insight into the both the validity of the neoclassical calculation and the amount of transport that can be attributed to neoclassical effects. Neoclassical predictions have been calculated by both the GSRAKE code (see Ref. 28,29) and the FORTEC-3D code (see Ref. 30,31). Both of these codes find the radial electric field (E_r) required to achieve an ambipolar particle flux in stellarator geometries. The predicted neoclassical radial electric field and predicted heat flux from these codes is shown in Fig.3 and Fig.5 respectively. When comparing these neoclassical predictions to experimental quantities, it is important to note that neither GSRAKE or FORTEC-3D include impurity species (such as argon) in any of the calculations.

The GSRAKE code is based on a general solution of the ripple-averaged kinetic equation. This treatment is valid only in the case of simple stellarator geometry, of which LHD qualifies. Details on the applicability of GSRAKE to LHD, and comparisons against other calculation techniques are detailed in Ref. 32.

FORTEC-3D uses a Monte-Carlo particle following approach, allowing it to use fewer assumptions and account for non-local finite orbit effects. For the results shown in this work, a new technique was used that allowed FORTEC-3D to calculate both the ion and electron particle fluxes for a self consistent solution for the radial electric field and other neoclassical transport parameters. This calculation is done by first calculating a guess of the radial electric field E_{r0} using a local code for the electron fluxes and FORTEC-3D for the ion particle fluxes. The initial guess is obtained by solving the time evolution of E_r according to the radial current, $dE_r/dt = -\frac{e}{\epsilon_\perp \epsilon_0}(Z_i\Gamma_I - \Gamma_e)$, where Γ denotes the particle fluxes and $\epsilon_\perp$ denotes the effect of the classical polarization current (see Ref. 9). A series of E_r profiles are then created based on this initial guess, $E_{r0} \pm \Delta E$, and FORTEC-3D is run on each E_r profile in this series to calculate both ion and electron fluxes. This provides the dependence of the particle flux as a function of E_r at each point in the plasma. Finally the ambipolar solution is found by fitting the E_r dependence of the difference in particle fluxes ($Z_I\Gamma_I - \Gamma_e$)

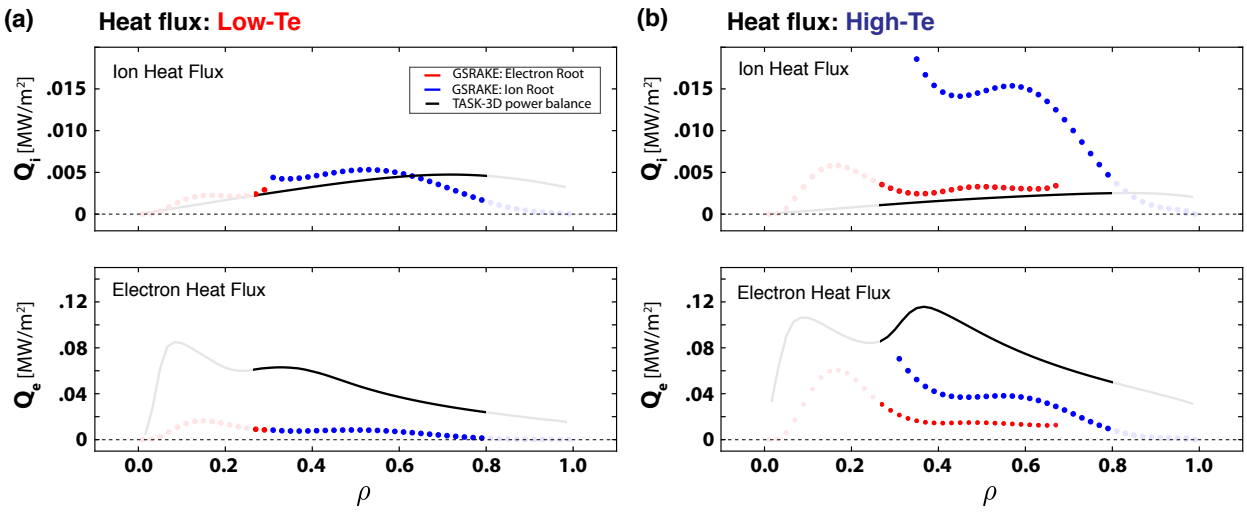

FIG. 5. Transport analysis showing ion and electron heat fluxes during the low-T_e and high-T_e phases of shot 114722. The black line shows TASK3D power balance calculations. The red points represent the GSRAKE neoclassical electron-root solution, while the blue points represent the ion-root solution; the unstable solution is not shown. The low-T_e plots use profiles from $3500ms$, the high-T_e plots use profiles $3700ms$ for the power balance results and $4000ms$ for the neoclassical calculation. There are large uncertainties in the neoclassical calculations and flux surface geometry for $\rho < 0.3$, and ion temperature measurements are not available for $\rho > 0.8$, therefore these regions have been deemphasized.

and finding the zero crossing. Compared to a local neoclassical solution like GSRAKE, this method importantly includes the higher-order effects such as the ion finite-orbit-width and E_r-shear on the neoclassical flux. In the FORTEC-3D results shown in Fig.3, the calculation between $\rho = 0.75$ and $\rho = 0.85$ has a high uncertainty because the particle fluxes calculated by FORTEC-3D become insensitive to the radial electric field in this region.

III. RESULTS

The power balance analysis of this discharge focuses on three times, $3500ms$, $3700ms$ and $4100ms$. The first time is during the low-T_e phase, while the later two times are both in the high-T_e phase, before and after the NBI injection (as described in Section II E). For the analysis of both the low-T_e and high-T_e cases, the plasma has not completely reached a steady state in terms of the electron temperature and density profiles, however the stored energy evolution terms have been examined and are have a small effect on the electron power balance. More importantly, the perpendicular flow profile is fully evolved giving confidence that the results capture the essential transport properties at the analysis times.

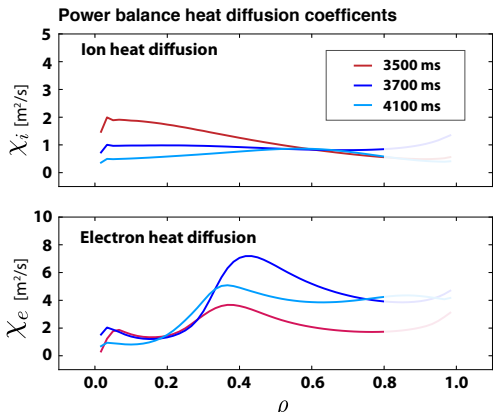

FIG. 6. Effective thermal diffusion coefficients for ions and electrons calculated for 114722 at $3500ms$, $3700ms$ and $4100ms$ as determined from power balance.

The power balance calculations performed using TASK3D assume thermalized electron and ion distributions at the chosen analysis times (when the neutral beams are not active). This assumption is supported by the close agreement between the kinetic energy, calculated using the measured temperature and density profile, and the stored energy measured by the diamagnetic loop (see Fig.1(b)). This agreement provides confidence that at the analysis times there are no fast ion or fast electron populations that need to be considered, and that the argon and hydrogen temperatures are the same.

The ion and electron heat flux calculated by TASK3D are shown in Fig.5, and compared with neoclassical predictions from GSRAKE. The range inside of $\rho < 0.3$ has been deemphasised due uncertainties in the neoclassical calculations of the heat fluxes and in the calculation of the flux surface geometry. The range outside of $\rho < 0.8$ has also been deemphasized due to unavailability of ion temperature measurements in this range.

Both the electron root and the ion root solutions from GSRAKE are shown. The perpendicular velocity measurements shown in Fig.3 can be used to determine that during the high-T_e phase the electron root solution should be chosen wherever two solutions exist. This choice is also supported by the agreement between in the ion heat flux between the power balance analysis and the neoclassical electron root solution; the ion root solution, with $Q_{\text{Neoclassical}} > Q_{\text{PowerBalance}}$, is not physically realistic.

For the ions, the experimental heat fluxes are approximately the same as the neoclassical predictions over most of the plasma (when choosing the electron root solution). This suggests that the ion heat flux is dominated by neoclassical effects. The uncertainties in the

calculation of the both the neoclassical results and the experimental ion heat flux are likely larger than the discrepancy seen in the values, particularly since the stored energy evolution was not included in the power balance calculation.

For the electrons, the neoclassical electron heat flux is nearly an order of magnitude lower than the measured heat flux in both the low and high T_e phases. This is an indication that electron transport is almost entirely dominated by turbulent sources in the range $0.3 < \rho < 0.8$ where power balance and neoclassical calculations are available without large uncertainties. After the transition to the high-T_e phase, an increase in the electron heat flux is seen in both the neoclassical and experimental heat fluxes, however because of the uncertainties in both calculations it is not possible to draw strong conclusions about the source of this increase, weather neoclassical or turbulent.

Calculation of the effective thermal diffusion coefficients during the low-T_e and high-T_e phases are shown in Fig.6. These effective diffusion coefficients have been calculated from the heat fluxes though the relation $Q_s = -n\chi_s \frac{\partial T_s}{\partial r}$, where the subscript s refers to either ions or electrons. Even before entering the high-T_e phase, the electron thermal diffusion coefficient, χ_e shows a region of reduced transport inside of $\rho = 0.4$. During the high-T_e phase, this reduced transport region is maintained, while outside of this region the transport is increased. This behavior can be seen in the electron temperature profile where the temperature and temperature gradient increase dramatically inside of $\rho = 0.4$, but change more modestly outside of this region. The majority of the electron heating is deposited in the core region of the plasma.

The ion temperature decreases only slightly between the low and high T_e phases. Without neutral beam injection, the only power being deposited to the ions is from electron-ion collisional thermal transfer. This transfer has a dependency on the electron temperature that goes as approximately $n_e^2 T_e^{-1/2}$, when $T_i << T_e$ as in the present case, and therefore there is less heating of the ions as the electron temperature increases and density decreases (see Fig.4). Since there are only small changes in the ion temperature, or ion temperature gradient, this is seen as a reduction in the ion thermal diffusion coefficient, χ_i.

Measurements of the perpendicular flow can give us some insight into how the radial electric field changes during the transition to the high-T_e phase. The perpendicular velocity

can be related to the radial electric field through the force balance equation[33–35].

$$E_r = \frac{1}{e n_I Z_I} \frac{\partial p_I}{\partial r} - u_\perp B \tag{2}$$

where r is in a direction normal to the magnetic flux surface, the subscript I denotes the ion species, n_I is the ion density, Z_I is the charge, p_I is the pressure, $u_\perp$ is the velocity perpendicular to the magnetic field, and B is the magnetic field. The diamagnetic drift term (pressure gradient) is typically quite small in stellarator plasmas, especially in the case of argon which has a large value of Z. This allows us to relate, qualitatively, the radial electric field profile directly to the measurement of the perpendicular velocity. The perpendicular flow measurements, taken from the XICS system, show an expansion of the electron root region from the core region inside of $\rho = 0.3$ (low-T_e phase) to the entire plasma out to $\rho \geq 0.8$ (high-T_e phase), see Fig.3.

These measurements are consistent with the neoclassical calculations of E_r from GSRAKE and FORTEC-3D. Inside of $\rho = 0.3$ GSRAKE finds a single electron root solution, with a positive radial electric field, to exist for both the low-T_e and high-T_e phases of this shot. During the low-T_e phase, GSRAKE only finds a single ion root solution outside of $\rho = 0.3$, with a small negative E_r. After the transition to the high-T_e phase an electron root solution, with a large positive E_r, is also found as a possible solution over most of the core plasma, out to approximately $\rho = 0.7$. Similarly FORTEC-3D predicts an electron root solution out to $\rho = 0.8$, which is in general agreement with the rotation measurements.

A comparison of the radial electric field inferred from the perpendicular flow measurements with the neoclassical predictions is also shown in Fig.3. In inferring E_r from $u_\perp$, the diagmagnetic drift term in Eq.2 is neglected, and only the $u \times B$ term is used. In evaluating this comparison it is important to keep in mind that both the inferred and neoclassical values are approximations; in particular the measured rotation is for argon, while the neoclassical calculations are done for a pure hydrogen plasma. Nonetheless the shape of the rotation profile and the magnitude of the flow velocity are reasonably well matched, particularly in the plasma core, providing confidence in the neoclassical calculations.

IV. CONCLUSION

A detailed study of a high-T_e ECH-only heated discharge on LHD has been completed. The discharge transitions from a state with a localized core electron-root E_r, to a global ($\rho \lesssim 0.8$) electron-root E_r, with a corresponding increase in the central electron temperature. The use of the XICS diagnostic along with the TASK3D suite has allowed the radial electric field structure to be inferred, as well as the both the ion and electron heat transport profiles.

The current results are consistent with the previous results on LHD from NBI sustained plasmas with ECH heating, such as in Ref. 6–8. The current results, which focus on purely ECH heated plasmas, allow for a simplified power balance to be completed which need not consider neutral beam power deposition. The final determined central value for the electron thermal diffusion coefficient during the high-T_e phase is similar between the current and previous studies. Previous studies however have focused on the electron transport properties, and have not reported ion heat transport results. The current results suggest that electron heat transport is dominated by turbulent sources while ion heat transport is of the same magnitude and may be consistent with neoclassical calculations during all portions of the analyzed discharge.

Previous studies on LHD, in particular the work done in Ref. 8, indicate that the injection of neutral beams has a very significant effect on the behavior of these high-T_e core electron root plasmas. In particular whether the beams are injected in the co-rotating or counter-rotating direction affects both the radial electric field structure and the confinement properties. The current results provide a case without neutral beams, which provides an additional data set without external momentum or current input for a similarly configured plasma. In this case we find behavior that is more similar to that of the counter-current NBI injection case.

The observed outward expansion of the localized core radial electric field with the addition of ECH power, seen in the current work, has not been previously studied on LHD. This adds to our understanding of the radial electric field from the previous studies, which largely focused on the transition from ion-root to core electron-root, and provides a more complete picture the role of the radial electric field in producing an internal transport barrier.

The current results also compare well with previous studies on high-T_e plasmas in the W7-AS stellarator with pure ECH heating (see Ref. 36). The predicted shape of the neo-

classical radial electric field in W7-AS is consistent with the current measurements of the perpendicular flow on LHD. In addition, the radial profile of the electron diffusion coefficient found through power balance is also similar between the current work and the previous study. This suggests that the current results are applicable more generally to helical devices, and that the predictive tools can be applied to the study of future machines.

Measurements of the perpendicular flow show qualitatively good agreement with neoclassical calculations of the radial electric field from FORTEC-3D and GSRAKE both in the low-T_e and high-T_e phases of this shot. This gives additional confidence to previously reported results for high-T_e plasmas with only ECH heating, such as in Ref. 9, as well as confidence in future studies using these software tools. The current results are well suited to comparisons with neoclassical predictions as no external momentum or core particle fueling inputs need be considered. Future studies will allow this evolution to be more carefully measured and provide more direct quantitative comparisons with the theoretical results.

Finally the current capabilities of the TASK3D suite for use in stellarator/heliotron transport research have been highlighted. This framework will be used for future transport studies to build further understanding of stellarator plasmas and the role of neoclassical transport.

Research supported by the U.S. DOE under Contract No. DE-AC02-09CH11466 with Princeton University. Development of TASK3D is supported by NIFS collaborative Research Programs NIFS14KNTT025. Part of simulations have been carried out on Plasma Simulator in NIFS under the support by NIFS collaborative Research Programs NIFS13KNST051.

REFERENCES

[1]M. Yokoyama, C. Suzuki, R. Seki, M. Osakabe, M. Yoshinuma, M. Sato, A. Wakasa, S. Murakami, A. Fukuyama, Y. Suzuki, K. Ida, H. Lee, and the LHD experiment group, Plasma and Fusion Research **8**, 2403016 (2013).

[2]N. A. Pablant, M. Bitter, L. Delgado-Aparicio, M. Goto, K. Hill, S. Lazerson, S. Morita, A. Roquemore, D. Gates, D. Monticello, G. H. Nielson, A. Reiman, M. Reinke, J. Rice, and H. Yamada, Review of Scientific Instruments **83**, 083506 (2012).

[3]M. Yokoyama, H. Maaßberg, C. Beidler, V. Tribaldos, K. Ida, T. Estrada, F. Castejon, A. Fujisawa, T. Minami, T. Shimozuma, Y. Takeiri, A. Dinklage, S. Murakami, and

H. Yamada, Nuclear Fusion **47**, 1213 (2007).

[4]M.Yokoyama, O.Yamagishi, K.Ida, M.Yoshinuma, Y.Takeiri, S.Morita, H.Funaba, K.Nagaoka, O. Kaneko, and the LHD Experimental Group, Proceedings of the 17th International Toki Conference , P1 (2007).

[5]Y. Takeiri, T. Shimozuma, S. Kubo, S. Morita, M. Osakabe, O. Kaneko, K. Tsumori, Y. Oka, K. Ikeda, K. Nagaoka, N. Ohyabu, K. Ida, M. Yokoyama, J. Miyazawa, M. Goto, K. Narihara, I. Yamada, H. Idei, Y. Yoshimura, N. Ashikawa, M. Emoto, H. Funaba, S. Inagaki, M. Isobe, K. Kawahata, K. Khlopenkov, T. Kobuchi, A. Komori, A. Kostrioukov, R. Kumazawa, Y. Liang, S. Masuzaki, T. Minami, T. Morisaki, S. Murakami, S. Muto, T. Mutoh, Y. Nagayama, Y. Nakamura, H. Nakanishi, Y. Narushima, K. Nishimura, N. Noda, S. Ohdachi, T. Ozaki, B. J. Peterson, A. Sagara, K. Saito, S. Sakakibara, R. Sakamoto, M. Sasao, K. Sato, M. Sato, T. Seki, M. Shoji, H. Suzuki, N. Tamura, K. Tanaka, K. Toi, T. Tokuzawa, K. Y. Watanabe, T. Watari, Y. Xu, H. Yamada, M. Yoshinuma, K. Itoh, K. Ohkubo, T. Satow, S. Sudo, T. Uda, K. Yamazaki, Y. Hamada, K. Matsuoka, O. Motojima, M. Fujiwara, T. Notake, N. Takeuchi, Y. Torii, S. Yamamoto, T. Yamamoto, T. Akiyama, P. Goncharov, T. Saida, H. Kawazome, and H. Nozato, Physics of Plasmas **10**, 1788 (2003).

[6]T. Shimozuma, S. Kubo, H. Idei, Y. Yoshimura, T. Notake, K. Ida, N. Ohyabu, I. Yamada, K. Narihara, S. Inagaki, Y. Nagayama, Y. Takeiri, H. Funaba, S. Muto, K. Tanaka, M. Yokoyama, S. Murakami, M. Osakabe, R. Kumazawa, N. Ashikawa, M. Emoto, M. Goto, K. Ikeda, M. Isobe, T. Kobichi, Y. Liang, S. Masuzaki, T. Minami, J. Miyazawa, S. Morita, T. Morisaki, T. Mutoh, H. Nakanishi, K. Nishimura, N. Noda, S. Ohdachi, Y. Oka, T. Ozaki, B. J. Peterson, Y. Narushima, A. Sagara, K. Saito, S. Sakakibara, R. Sakamoto, M. Sasao, M. Sato, K. Satoh, T. Seki, S. Shoji, H. Suzuki, N. Tamura, K. Tokuzawa, Y. Torii, K. Toi, K. Tsumori, K. Y. Watanabe, T. Watari, S. Yamamoto, T. Yamamoto, M. Yoshinuma, K. Yamazaki, S. Sudo, K. Ohkubo, K. Itoh, A. Komori, H. Yamada, O. Kaneko, Y. Nakamura, K. Kawahata, K. Matsuoka, O. Motojima, and the LHD Experimental Group, Plasma Physics and Controlled Fusion **45**, 1183 (2003).

[7]K. Ida, S. Inagaki, T. Shimozuma, N. Tamura, H. Funaba, K. Narihara, S. Kubo, S. Murakami, A. Wakasa, M. Yokoyama, Y. Takeiri, K. Y. Watanabe, K. Tanaka, M. Yoshinuma, Y. Liang, N. Ohyabu, T. Akiyama, N. Ashikawa, M. Emoto, T. Fujita, T. Fukuda, P. Goncharov, M. Goto, H. Idei, K. Ikeda, A. Isayama, M. Isobe, O. Kaneko, K. Kawa-

hata, H. Kawazome, T. Kobuchi, A. Komori, R. Kumazawa, S. Masuzaki, T. Minami, J. Miyazawa, T. Morisaki, S. Morita, S. Muto, T. Mutoh, Y. Nagayama, Y. Nakamura, H. Nakanishi, Y. Narushima, K. Nishimura, N. Noda, T. Notake, H. Nozato, S. Ohdachi, Y. Oka, S. Okajima, M. Osakabe, T. Ozaki, B. J. Peterson, A. Sagara, T. Saida, K. Saito, S. Sakakibara, R. Sakamoto, Y. Sakamoto, M. Sasao, K. Sato, M. Sato, T. Seki, M. Shoji, H. Suzuki, N. Takeuchi, K. Toi, T. Tokuzawa, Y. Torii, K. Tsumori, T. Watari, H. Yamada, I. Yamada, S. Yamamoto, T. Yamamoto, Y. Yoshimura, K. Itoh, K. Matsuoka, K. Ohkubo, S. Sudo, T. Uda, K. Yamazaki, and O. Motojima, Physics of Plasmas **11**, 2551 (2004).

[8]T. Shimozuma, S. Kubo, H. Idei, S. Inagaki, N. Tamura, T. Tokuzawa, T. Morisaki, K. Watanabe, K. Ida, I. Yamada, K. Narihara, S. Muto, M. Yokoyama, Y. Yoshimura, T. Notake, K. Ohkubo, T. Seki, K. Saito, R. Kumazawa, T. Mutoh, T. Watari, A. Komori, and the LHD Experimental Group, Nuclear Fusion **45**, 1396 (2005).

[9]S. Matsuoka, S. Satake, H. Takahashi, A. Wakasa, M. Yokoyama, T. Ido, A. Shimizu, T. Shimozuma, S. Murakami, and LHD Experiment Group, Plasma and Fusion Research **8**, 1403039 (2013).

[10]H. Takahashi, T. Shimozuma, S. Kubo, Y. Yoshimura, H. Igami, S. Ito, S. Kobayashi, Y. Mizuno, K. Okada, T. Mutoh, K. Nagaoka, S. Murakami, M. Osakabe, I. Yamada, H. Nakano, M. Yokoyama, T. Ido, A. Shimizu, R. Seki, K. Ida, M. Yoshinuma, T. Kariya, R. Minami, T. Imai, N. B. Marushchenko, Y. Turkin, and L. E. Group, Physics of Plasmas **21**, 061506 (2014).

[11]I. Yamada, K. Narihara, H. Funaba, T. Minami, H. Hayashi, T. Kohmoto, and L. E. Group, Fusion Science and Technology **58**, 345 (2010).

[12]N. B. Marushchenko, V. Erckmann, H. J. Hartfuss, M. Hirsch, H. P. Laqua, H. Maassberg, and Y. Turkin, Plasma and Fusion Research **2**, S1129 (2007).

[13]T. Shimozuma, H. Takahashi, S. Kubo, Y. Yoshimura, H. Igami, M. Nishiura, S. Ogasawara, R. Makino, H. Idei, N. B. Marushchenko, Y. Turkin, and T. Mutoh, Plasma and Fusion Research **8**, 2402073 (2013).

[14]Yokoyama, M. for TASK3D Users and Developers, memo 61 (NIFS, 2012).

[15]A. Wakasa, A. Fukuyama, S. Murakami, M. Miki, M. Yokoyama, M. Sato, S. Toda, H. Funaba, K. Tanaka, K. Ida, H. Yamada, M. Honda, and N. Nakajima, in *23rd IAEA Fusion Energy Conf.* (2010).

[16]N. A. Pablant, R. E. Bell, M. Bitter, L. Delgado-Aparicio, K. W. Hill, S. Lazerson, and S. Morita, Review of Scientific Instruments **85**, 11E424 (2014).

[17]J. Arévalo, J. Alonso, K. McCarthy, and J. Velasco, Nuclear Fusion **53**, 023003 (2013).

[18]K. Kawahata, K. Tanaka, Y. Ito, A. Ejiri, and S. Okajima, Review of Scientific Instruments **70**, 707 (1999).

[19]S. Hirshman and W. van Rig, Computer Physics Communications **43**, 143 (1986).

[20]S. Lazerson, D. Gates, D. Monticello, H. Neilson, N. Pomphrey, A. Reiman, S. Sakakibara, and Y. Suzuki, in *Europhysics Conference Abstracts*, Vol. 35G (2011) p. O5.417, 38th EPS Conference on Plasma Physics.

[21]S. Lazerson and the DIII-D Team, Nuclear Fusion **55**, 023009 (2015).

[22]J. Huba, *NRL Plasma Formulary* (Naval Research Laboratory, 2013).

[23]S. Kubo, H. Idei, T. Shimozuma, Y. Yoshimura, T. Notake, K. Ohkubo, S. Inagaki, Y. Nagayama, K. Narihara, and The Lhd Experiment Group, J. Plasma Fusion Res. SERIES **5**, 584 (2002).

[24]S. Kubo, H. Idei, T. Shimozuma, Y. Yoshimura, T. Notake, K. Ohkubo, S. Inagaki, Y. Nagayama, K. Narihara, I. Yamada, S. Muto, S. Morita, and L. E. Group (LHD Experimental Group), AIP Conference Proceedings **669**, 187 (2003).

[25]A. Bustos, F. Castejón, M. Osakabe, L. Fernández, V. Martin-Mayor, J. Guasp, and J. Fontdecaba, Nuclear Fusion **51**, 083040 (2011).

[26]B. J. Peterson, A. Y. Kostrioukov, N. Ashikawa, Y. Liu, Y. Xu, M. Osakabe, K. Y. Watanabe, T. Shimozuma, S. Sudo, and the LHD Experiment Group, Plasma Physics and Controlled Fusion **45**, 1167 (2003).

[27]T. Morisaki, K. Oyama, N. Tamura, S. Masuzaki, T. Akiyama, G. Motojima, J. Miyazawa, B. Peterson, N. Ohno, and H. Yamada, Journal of Nuclear Materials **463**, 640 (2015), pLASMA-SURFACE {INTERACTIONS} 21Proceedings of the 21st International Conference on Plasma-Surface Interactions in Controlled Fusion Devices Kanazawa, Japan May 26-30, 2014.

[28]C. D. Beidler and W. D. D'haeseleer, Plasma Physics and Controlled Fusion **37**, 463 (1995).

[29]C. D. Beidler and H. Maaßberg, Plasma Physics and Controlled Fusion **43**, 1131 (2001).

[30]S. Satake, M. Okamoto, N. Nakajima, H. Sugama, M. Yokoyama, and C. Beidler, Nuclear Fusion **45**, 1362 (2005).

[31]S. Matsuoka, S. Satake, M. Yokoyama, A. Wakasa, and S. Murakami, Physics of Plasmas

18, 032511 (2011).

[32]C. Beidler, K. Allmaier, M. Isaev, S. Kasilov, W. Kernbichler, G. Leitold, H. Maaßberg, D. Mikkelsen, S. Murakami, M. Schmidt, D. Spong, V. Tribaldos, and A. Wakasa, Nuclear Fusion **51**, 076001 (2011).

[33]K. Ida, Plasma Physics and Controlled Fusion **40**, 1429 (1998).

[34]J. D. Callen, A. J. Cole, and C. C. Hegna, Physics of Plasmas (1994-present) **16**, 082504 (2009).

[35]H. Ehmler, J. Baldzuhn, K. McCormick, A. Kreter, T. Klinger, and W.-A. Team, Plasma Physics and Controlled Fusion **45**, 53 (2003).

[36]M. Romé, C. D. Beidler, H. Maaßberg, N. B. Marushchenko, Y. A. Turkin, and the W7-AS Team, Plasma Physics and Controlled Fusion **48**, 353 (2006).